EUROFUSION WPMST1-CP(16) 15128

HF Meyer et al.

Overview of progress in European Medium Sized Tokamaks towards an integrated plasma-edge/wall solution

Preprint of Paper to be submitted for publication in
Proceedings of 26th IAEA Fusion Energy Conference

This work has been carried out within the framework of the EUROfusion Consortium and has received funding from the Euratom research and training programme 2014-2018 under grant agreement No 633053. The views and opinions expressed herein do not necessarily reflect those of the European Commission.

Overview of progress in European Medium Sized Tokamaks towards an integrated plasma-edge/wall solution

H. Meyer[1], T. Eich[2], M. Beurskens[3], S. Coda[4], A. Hakola[5], P. Martin[6] and the ASDEX Upgrade, MAST, TCV and EUROfusion MST1 ‡ Teams

[1]CCFE, Culham Science Centre, Abingdon, Oxon, OX14 3DB, UK; [2]Max-Planck-Institut für Plasmaphysik, D-85748 Garching, Germany; [3]Max-Planck-Institut für Plasmaphysik, Teilinstitut Greifswald, D-17491 Greifswald, Germany; [4]Ecole Polytechnique Fédérale de Lausanne (EPFL), Swiss Plasma Center (SPC), CH-1015 Lausanne, Switzerland; [5]VTT Technical Research Centre of Finland, P.O.Box 1000, FI-02044 VTT, Finland; [6]Consorzio RFX, corso Stati Uniti 4, 35127 Padova, Italy
E-mail: Hendrik.Meyer@ccfe.ac.uk

Abstract: Integrating the plasma core performance with an edge and scrape-off layer (SOL) that leads to tolerable heat and particle loads on the wall is a major challenge. The new European Medium Size Tokamak Task Force (EU-MST) coordinates research on ASDEX Upgrade (AUG), MAST and TCV. This multi-machine approach within EU-MST covering a wide parameter range is instrumental to progress the field, as ITER and DEMO core/pedestal and SOL parameters are not achievable simultaneously in present day devices. A two prong approach is adopted. On the one hand scenarios with tolerable transient heat and particle loads including active ELM control are developed. On the other hand divertor solutions including advanced magnetic configurations are studied. Considerable progress has been made on both approaches, in particular in the fields of: ELM control with resonant magnetic perturbations, small ELM regimes, detachment onset and control as well as filamentary scrape-off-layer transport. For example full ELM suppression has now been achieved on AUG at low collisionality with $n = 2$ RMP maintaining good confinement $H_{\mathrm{H(98,y2)}} \approx 0.95$. Advances have been made with respect to detachment onset and control. Studies in advanced divertor configurations (Snowflake, Super-X and X-point divertor) shed new light on SOL physics. Cross field filamentary transport has been characterised in a wide parameter regime on AUG, MAST and TCV progressing the theoretical and experimental understanding crucial for predicting first wall loads in ITER and DEMO. SOL condition also play a crucial role for ELM stability and access to small ELM regimes.

1 Introduction: One of the key challenges towards the realisation of a magnetic confinement fusion power plant is to integrate the high-confinement core with the edge of the plasma such that acceptable wall conditions are obtained whilst maintaining the high performance. In particular the periodic transient heat loads due to edge localised modes (ELM) [1, 2] in the otherwise promising high confinement mode will not be tolerable in ITER and DEMO [3]. Cyclic thermo-mechanical loads may limit the number and size of ELMs to much smaller values than a design criteria to prevent melt damage, especially in DEMO. For the achievement of physics understanding of the plasma edge and the ability to extrapolate the findings to future devices, a wide parameter range needs to be investigated. This is a task ideally suited to the new European task force on Medium Sized Tokamaks (EU-MST) that has combined research on three key, complementary devices ASDEX Upgrade (AUG), TCV and MAST since 2014.

‡ see Appendix 1: The EUROfusion MST1 Team

Research under the EU-MST task force tackles the edge challenge from two sides. On the one hand plasma regimes reducing the transient heat loads whilst trying to maintain high confinement are developed with active ELM control techniques (Sec. 2) and natural small ELM scenarios (Sec. 3). On the other hand divertor solutions with detachment control (Sec. 4) and advanced magnetic configurations (Sec. 5) are studied. In this paper we will give an overview of the progress made in the last two years in these two research fields within EU-MST supported by the domestic programs. In addition, we will discuss the enhanced filamentary radial transport in the scrape-off layer (SOL) becoming more important as transient heat loads on the divertor targets are reduced (Sec. 6). Studies have been performed in D, H and He as the main discharge species to assess the feasibility of the methods for the non-nuclear phase in ITER.

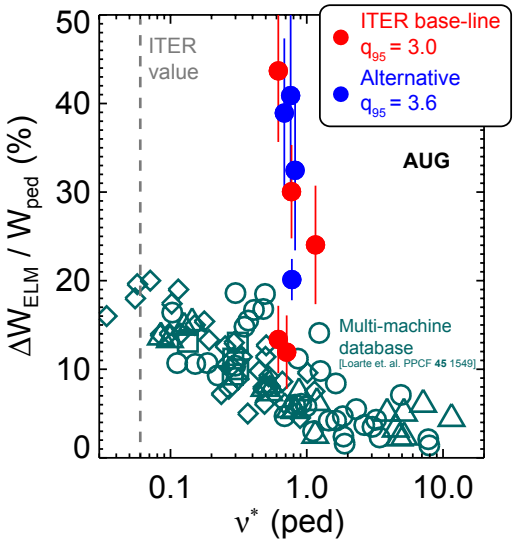

Figure 1: *Relative ELM energy loss of the ITER base-line scenario at $q_{95} = 3$ (red) and its $q_{95} = 3.6$ (blue) variant in comparison to the ν^* scaling from[4].*

2 Reducing the ELM size with actuators Approximations to the ITER baseline scenario on AUG ($3 \leq q_{95} \leq 3.6$, $n/n_G = 0.85$, $\beta_N = 1.8$) show that the low q_{95} and high triangularity lead to low frequency ELMs with exceptionally large energy loss of up-to 45% of the pedestal energy on AUG [5] (see Fig. 1), though these large ELMs may be multiple events. The relative ELM energy losses in the AUG variant of the ITER base-line scenario lie well above the scaling from Loarte et.al. [4]. Gas fuelling can reduce the ELM size, but will lead to a degradation of the confinement due to the erosion of pedestal pressure as also seen on JET [6]. A likely reason for this reduction in p_{ped} is the presence of a high density front at the high field side [7], which leads to an outward shift of the density pedestal in turn leading to a reduction of the peeling-ballooning stability. The scenario also has proven resilient to active ELM mitigation techniques such as pellet triggering or application of resonant magnetic perturbations (RMP). Application to RMPs have lead to a clear,though small density pump-out, but not an increase of ELM frequency or reduction in ELM energy loss. Interestingly, a slight vertical upshift approaching a double null configuration or reduction in divertor pumping gives access to a small ELM regime not unlike the type-II ELM regime (see Sec. 3) [8, 5]. Assessing the performance of the ITER base-line scenario and its variant in high purity He plasmas ($n_{He}/(n_{He}+n_H+n_D) \gtrsim 80\%$) shows a similar ELM behaviour with larger ELMs $\Delta W_{ELM} \approx 50$ kJ ($\Delta W_{ELM}/W_{pl} \approx 10\%$) at lower neutral density and small ELMs at high neutral density. The new neutral beam injection on TCV has enabled studies of these high density regime on TCV and scenario development has been started.

For single events, the peak parallel ELM energy fluence, $\varepsilon_{||}(s) = \varepsilon_{div}/\sin\alpha_{div} = f_x(B_t/B_p)\int q(s,t)dt$ (f_x: flux expansion, q heat flux, α_{div} field line angle on the target), of natural type-I ELMs on ASDEX Upgrade and JET never exceeds a value proportional

to the pedestal top pressure, p_e^{ped}, times the geometric minor radius, a [9]. This data set has now been extended to MAST and discharges with active ELM control and will be extended to TCV in the future.

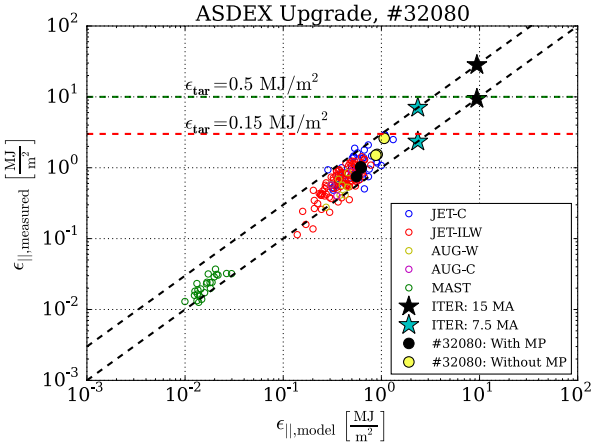

Figure 2: *Measured type-I peak ELM energy fluence against model prediction for a multi-machine database including AUG, JET and MAST.*

In Fig. 2 the comparison of the measured $\max(\varepsilon_{||})$ to a simple ad-hoc model of a toroidally symmetric reconnected flux tube $\max(\varepsilon_{||}^{\mathrm{model}}) = \Delta_{\mathrm{eqil.}} 2\pi a \sqrt{\frac{1+\kappa^2}{2}} \frac{3}{2} p_e^{\mathrm{ped}} \frac{B_t}{B_p}$ is shown (κ: elongation). Over two orders of magnitude the data is within a factor of three of this simple prediction giving a minimum value. The data set includes data from the inner and outer divertor of AUG as well as shots with ELM control using pellets and vertical kicks in the case of JET. Predictions for two ITER scenarios together with the current material limit are shown as well. In Fig. 2 data of an AUG discharge with RMPs at low collisionality are shown as well. As for the cases of ELM control in JET the RMP data fits into the overall trend. In detail the application of RMPs increases the ELM frequency on AUG, but also reduces the pedestal pressure due to the density pump out. It should be noted that this trend is only true for cases where the ELMs are still of type-I. It is unclear if ELM control/mitigation techniques for type-I ELMs will be able to move the ELM heat loads from the upper boundary to or below the lower boundary whilst maintaining the pedestal pressure in a robust way. In any case this data suggests that it is unlikely that type-I ELMs are acceptable for the Q=10 scenario in ITER.

In certain ELM cycles on MAST the density could be replaced by gas fuelling [10]. Similar studies have been performed on AUG using pellets fuelling under ITER like conditions [11]. In these experiments the full density pedestal could be recovered. To refuel a density pump-out of 30% the fuelling rate had to be increased by a factor of two. However, it was not possible to fully recover the loss of confinement as the increase of the density lead to a decrease of temperature and the pedestal pressure could only be partly restored. As increased gas fuelling also affects ELM stability [12, 13], degrades confinement [6, 7] and can be used to control the ELM frequency [14], the increased recycling due to the increased

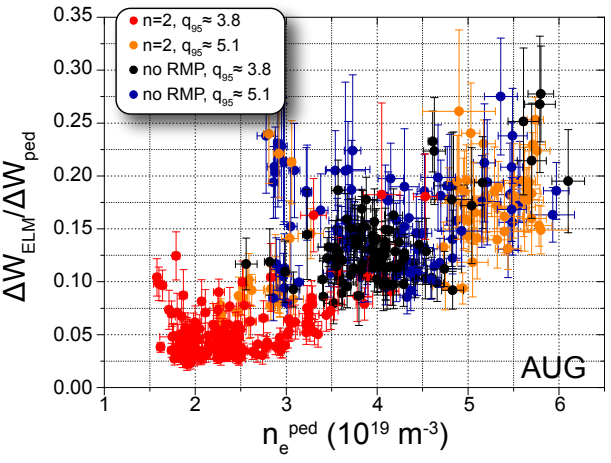

Figure 3: *Normalized ELM energy loss from function parameterisation equilibrium as function of electron density at the pedestal top before the ELM with and without RMP and two different edge safety factors.*

fuelling rate may also play a role in the loss of confinement. Pellet refuelling during RMPs did not trigger further ELMs and a mitigation of the ELM energy loss albeit at a compromised level was maintained. Within the error bars the peak heat load with and without pellets during the RMP phase did not change, but was only reduced by a factor of two in comparison to the pre RMP phase.

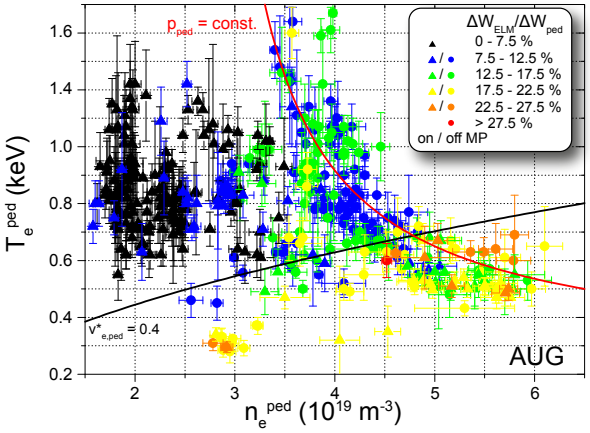

Figure 4: *Operating space in temperature and density for discharges with and without RMP for different ELM energy loss.*

The interplay between increased particle transport (e.g. density pump-out) and the efficiency ELM control at low collisionality is a key question for extrapolating to future devices that will have low collisionality at high Greenwald fraction [15]. Analysis of the AUG data base of low collisionality discharges using $n = 2$ RMP to affect the ELMs has shown that the ELM energy loss correlates best with the edge density (see Fig. 3) and less well with pedestal collisionality [16, 15]. However, a threshold of $\nu^*_{\rm ped} \lesssim 0.4$ has been found above which ELMs are not affected (Fig. 4). At the lowest edge density the loss of stored energy during an ELM can be reduced by 85%, but as can be seen from Fig. 4 not at an isobar corresponding to type I ELMy H-mode [16, 10]. At this parameter regime the low density branch of type III ELMs (also called type IV) is found on DIII-D [17] and MAST [10]. On DIII-D and MAST type-IV regimes can also be accessed without RMPs. Experiments with coil waveforms optimised to achieve a fast switch-off proved that on AUG it is not only the reduction in density that gives access to the small ELMs.

More recently ELM suppression was observed at low collisionality $\nu^\star_{\rm e,ped} \leq 0.25$ on AUG (see Fig. 5) [15] in a higher triangularity $\delta_{u/l} = 0.23/0.43$ DIII-D/AUG identity shape. The experiments on DIII-D revealed the crucial role of the triangularity for accessing full ELM suppression motivating the shape change on AUG. The suppression phase, starting at $t = 2.75$ s, is initiated by a reduction in gas fuelling leading to a drop in density between $t = 2.30 - 2.75$ s and is accompanied by a further, faster drop in density. Consequently, this leads to a drop in confinement by 25% with respect to the mitigated phase. However, the confinement soon recovers reaching stably $H_{\rm H(98y,2)} \lesssim 0.95$ from $t = 3.45$ s onwards. This is comparable to the ELM mitigation phase ($t = 2.5 - 2.75$ s), which in this

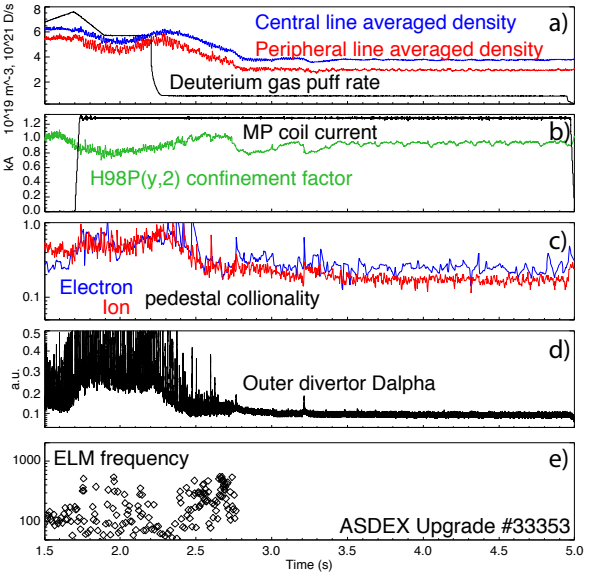

Figure 5: *Typical time traces for a low collisionality discharge on AUG were ELM suppression was achieved.*

shape has considerably higher confinement than in the low δ shape $\delta_{u/l} = 0.1/0.43$.

A key part of the RMP experiments under EU-MST was directed towards the understanding of the plasma response. Comparing the experimental data with plasma response calculations using the resistive MHD code MARS-F [18, 19, 20] confirmed the findings from MAST that the edge kink response needs to be maximised to affect the ELMs and is in good agreement with differential phase scans performed on AUG and MAST. The optimal phase angle for the applied perturbation depends roughly linearly on q_{95} [20] but also on β [21]. An analytical model based on dedicated scans of MARS-F starting from an example equilibrium has been developed to predict the phase angle prior to the experiments to within $\pm 20^\circ$ [21] by optimising the plasma response with respect to the displacement close to the X-point (kink response) and the perturbation at the outermost resonance. Measurements of the 3D perturbation of the plasma around the mid-plane using several diagnostics by rotating the perturbation field at constant phase angle between the upper and lower coils shows good agreement with the plasma response modelling using the 3D equilibrium code VMEC as well as MARS-F [22]. The perturbation was found to be non resonant $|m| > |nq|$, whilst the displacement is resonant $|m| = |nq|$ as predicted by the codes. The plasma response calculations have now been extended to the non-ideal MHD code JOREK [23] showing good agreement with VMEC and MARS-F calculations as well as qualitative agreement of the observed change in magnetic mode spectrum during the ELM [24] as well as the filamentary dynamics measured with ECE imaging [25].

ELM energy loss mitigation was also achieved in He discharges at low collisionality. The phase angle of the applied perturbation is similar to the one measured in D. Small differences may be explained by the lower β achieved in He. This shows that it should be possible to transfer the experience in He during the non-activation He phase on ITER to D. The ELMs are affected by the RMP in He at similar density as in D. However, the lower pedestal temperature in He leads to a much higher collisionality at which in D ELM control with RMPs is not possible. This suggests that the collisionality is not the only factor determining the effect of RMPs. It should be noted though that on MAST ELM mitigation can be achieved with almost all edge collisionalities [10]. For the higher collisionality ITER base-line scenarios pump-out as in D could be observed, but ELMs became larger at the lower density.

The physics of ELM energy loss mitigation at low and high collisionality on AUG is different. At high collisionality the RMP spectrum or alignment doesn't play a role [26]. Experiments at different plasma current and heating power showed that these mitigated ELMs are also likely a different ELM regime [27]. In contrast to the low collisionality regime however, this regime also persists without the magnetic perturbation (see Sec. 3).

The potential for ELM control with pellets in metal wall devices is greatly reduced due to a dead time after the previous ELM [28]. Injection of N recovers the trigger potential. Analysis of the inter ELM pedestal evolution on AUG shows that with and without N seeding ELMs can be triggered after the fast density recovery phase [29]. This may be related to the existence of long and short ELMs in all metal devices [30]. The long ELM

having an extra 2nd phase expelling filaments into the SOL [30] will degrade the pedestal more than the short ELM. Comparisons on AUG, JET and TCV of ELMs with and without N seeding seem to point at the crucial role of the SOL temperature [31] for the existence of the 2nd phase. It should be noted that the estimated $max(\varepsilon_{||})$ of N seeded ELMs is higher than of unseeded ELMs due to the faster deposition of the energy onto the target and the smaller wetted area. However, N also leads to earlier detachment of the divertor (see Sec. 4).

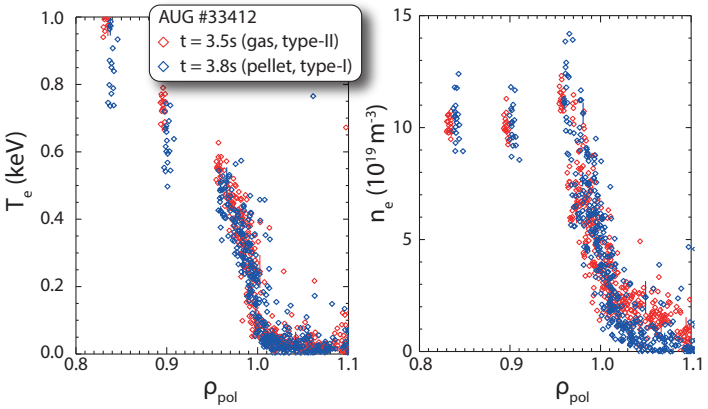

Figure 6: *Comparison of the electron temperature (left) and density (right) profiles in a gas fuelled phase (blue) and dominantly pellet fuelled phase (red) from Thomson scattering at otherwise constant discharge parameters.*

3 Small ELM regimes Not only type-I ELMs are affected by the SOL, also the onset of type-II ELMs is likely related to the SOL conditions. Comparison of the filamentary structure of type-II ELMs between AUG and MAST suggested the origin of the type-II ELM filaments to be at the foot of the pedestal [32]. Type-II and type-I ELMs can coexist giving further evidence for their different origin.

Recently the proximity of the ITER base-line scenario on AUG to small (type-II like) ELMs was discovered [5]. Replacing the gas fuelling in these discharges with pellet fuelling reduced SOL density as can be seen in Fig. 6 (right). The pedestal pressure was kept constant. Also the gradients of temperature and density are the same within the error bars in both phases. However, the pellet fuelled phase has type-I ELMs, whilst the gas fuelled phase exhibits small ELMs.

Experiments using $n = 2$ magnetic perturbations (MP) during strong fuelling ramps revealed the importance of the increasing intermittent transport for the occurence of small ELMs [27]. Discharges with three different plasma currents ($I_p = 0.6$, 0.8 and 1.0 MA) and two different heating levels ($P_{heat} = 6.3$ and 8.7 MW) were performed in order to try to separate collisionality from density. Here, type-I ELMs and small filaments coexist at lower fuelling levels and are fully replaced by small ELMs as the fuelling is increased. At the highest fuelling levels small ELMs persist even without MP. Hence, the MP is not necessary for the small ELMs to occur. With increasing fuelling n_e^{sep} and n_e^{ped} rise. With increasing $\nu^\star$ the filaments become larger and form the n_e shoulder in the SOL. The larger filaments occur together with a wider near SOL mid-plane T_e decay length, the pedestal becomes wider and due to the lower T_e^{ped}, and its gradient is shallower. The pedestal is (filamentary) transport limited and not peeling-ballooning limited as for type-I ELMs. The perturbation of the equilibrium by the MP leads to lobe structures clearly observable in the heat flux profile. Increased cross field transport due to the higher density (see Sec.6) populates lobes further away from the unperturbed separatrix as the fuelling is increased finally leading to the onset of detachment. The presence of the MP may influence the

density at which the cross field transport changes.

These results as well as the N seeding experiments point towards the importance of the SOL for the onset of small ELM regimes and the ELM stability as such. The SOL at high power high density discharges on AUG is closer to ITER/DEMO parameters than the SOL in low collisionality plasmas. To date it is unclear if the transport leading to the small ELM regime can be achieved at low collisionality and high density at the same time. Trying to decrease $\nu^\star$ in small ELM regimes by stronger heating usually leads to an increased density with a clamped pedestal temperature. The pedestal pressure achieved in these regimes is close to that of type-I ELMy H-mode.

The ELM energy loss is also reduced close to the density limit whilst maintaining high confinement. This phase has not yet been extended into a stable scenario, but the four phases of the H-mode density limit identified on AUG [33] have now also been observed on TCV despite the different divertor geometry.

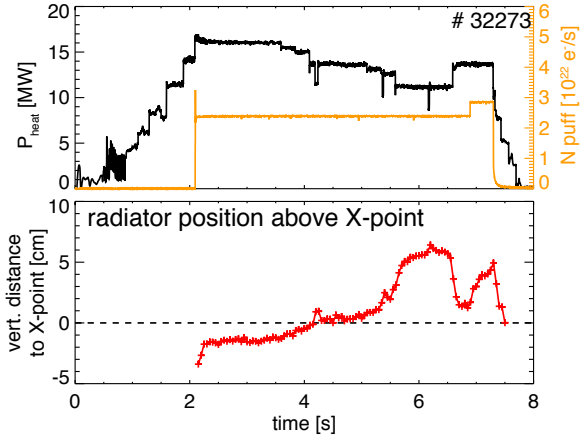

Figure 7: *Vertical position of the radiator relative to the X-Point in AUG #32273 with the modulation of heating power and N seeding.*

4 Buffering the divertor Partial detachment of the divertor is a key part of the integrated solution and has long been studied in conventional divertor configurations. Controlling the divertor temperature estimated from the thermal currents flowing in the SOL and using nitrogen influx as an actuator is well established on AUG [34]. This method may not be suitable for next step devices as it requires isolated tiles in a neutron environment and other observers may be needed for detachment control. Recently the position of a poloidally localised radiator close to the X-point, as measured by bolometry, has been identified as such a possible observer [35]. The time evolution of the vertical position of this X-point radiator for a discharge with varying heating power and N seeding is shown in Fig. 7 at high $P/R \lesssim 10\,\mathrm{MW/m}$. With a reduction of heating power, this radiator moves further inside the confined region and with an increase of the heating power, the equilibration point of the radiator moves closer to the X-point. The increase of the N seeding levels leads again to an inward movement. If the radiator moves too far inside the confined region, a disruption is triggered. The stability of the poloidal asymmetry is likely facilitated by the long connection length around the X-point. This is also observed in advanced divertor configurations (see Sec. 5).

Furthermore, different seeding gases (N, Ne, Ar, Kr) were used to control radiation in different areas of the plasma. Detached operation has been achieved with the highest $P/R \leq 15\,\mathrm{MW/m}$ at Greenwald fractions of $n_e/n_\mathrm{G} \approx 90\%$ and high $H_{\mathrm{H(98,y2)}} \lesssim 0.95$, though at high radiation and density $H_{\mathrm{H(98,y2)}}$ may not be the appropriate measure. A key point in understanding this physics is the accurate modelling of the fuelling sources and impurity transport in the SOL. Using the SOLPS5.0 code the high field side high

density region on AUG and the effect N seeding has on this front has been modelled [36]. Adapted diffusive and additional convective radial transport coefficients now reconcile the modeled deuterium compression ratio, divertor neutral density, neutral radiation levels and deuterium fueling rates with experimental measurements. The onset of strong volume recombination in the simulations now allows to remove the previously necessary increase of perpendicular transport in the inner divertor from the simulations.

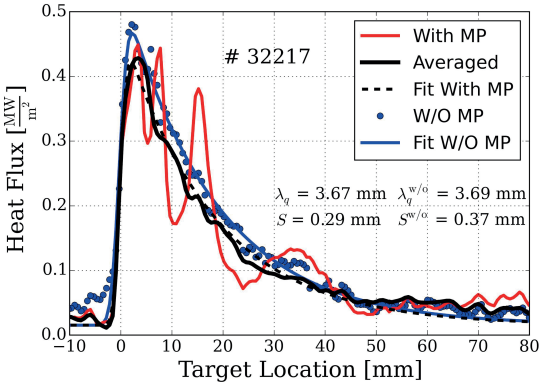

Figure 8: *L-mode heat flux profile on the outer divertor with MP (red) and without (blue). The toroidally averaged profile in the presence of MP (black) leads to the same distribution as the axisymmetric one.*

The application of 3D fields for ELM control will also impact on the divertor heat load, by breaking the toroidal symmetry leading to regions of increased heat load far from the strike point. Clear lobe structures are seen in the heat flux pattern at low and high collisionality on AUG and MAST. Using slowly rotating fields on AUG the toroidal variation of these patterns has been measured with IR imaging in L- and H-mode discharges with $n = 1,2,3$ RMPs [37]. In L-mode the heat flux profile averaged over a rotation of the perturbation by $2\pi/n$ will recover the unperturbed heat load profile (see Fig. 8) showing the cross field transport in L-mode is much higher than a potential effect due to the perturbation itself. Such transport could come from a stochastic layer. A new method to measure this layer using ECRH heat pulses in comparison with EMC3 modelling using an ad hoc screening model has been employed on AUG [38]. The analysis of L-mode discharges also showed no significant difference of the temporal behaviour of the heat pulse with and without RMPs.

5 Advanced divertors The work on detachment has been extended to the advanced divertor configurations studied experimentally on TCV [39, 40] and theoretically for MAST Upgrade geometry [41, 42]. These configurations aim to reduce the heat load of the target by geometrical means such as flux expansion as well as by increasing perpendicular transport and volumetric processes. EMC3-Eirene calculations of various TCV snowflake configurations for example predicted that a snowflake configuration with an additional X-point in the low field side SOL (SF-) would not only reduce the heat loads on the outer

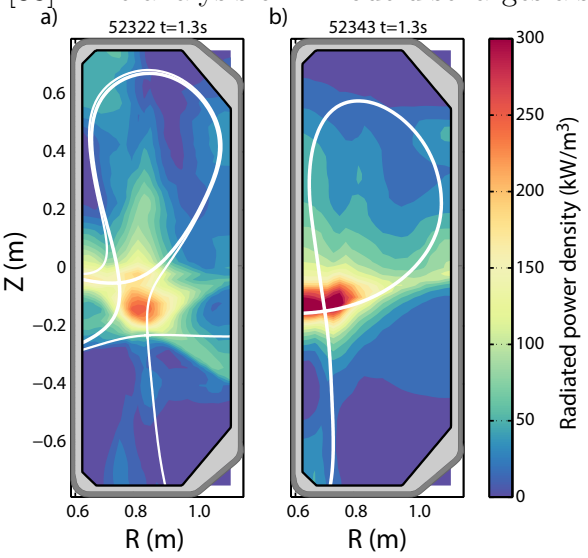

Figure 9: *Comparison of the tomographically inverted radiation in a) a LFS SF- and b) a conventional divertor configuration at similar discharge conditions and seeding levels*

target, but that impurity seeding should create a highly radiating zone trapped between the two X-points with a large volume [43].

This predicted trapped radiation zone has now been observed experimentally (see Fig. 9). With respect to power balancing however, fluid modelling is not able to reproduce the power distribution between the different strike points correctly when the secondary strike points are not connected to the SOL (SF^+). In particular more power than the modelling suggests arrives at the passive strike points in these snowflake configurations [44] and also double peaked profiles are observed [45]. Enhanced $E \times B$ drifts in the SF configuration could explain the power distribution. The $E \times B$ drifts are predicted to increase with density, increase with low distance between the X-points and reverse sign with B_t. All these predictions are in qualitative agreement with the measurements [44].

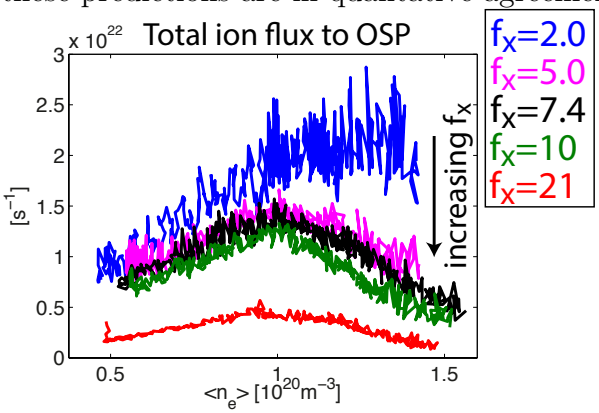

Figure 10: *Total ion flux to the outer divertor as a function of line averaged density for different poloidal flux expansions.*

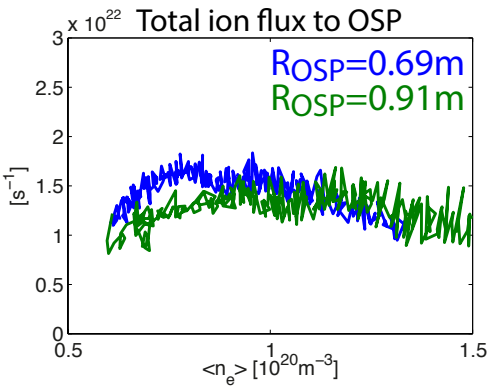

Figure 11: *Total ion flux to the outer divertor as a function of line averaged density for different total flux expansions (R_{OSP}).*

The dependence of the onset and the evolution of detachment on poloidal flux expansion (incl. strike point flaring "X-divertor") f_x, major radius R_{OSP} of the outer strike point (toroidal flux expansion,"Super-X"), the appearance of a 2nd X-point close to the target ("X-point divertor") at a particular $\rho_\psi = \sqrt{(\psi - \psi_0)/(\psi_a - \psi_0)}$ ($\psi_{0,a}$ poloidal flux at the separatix (a) and magnetic axis (0)) and vertical plasma height ($L||$) have been studied in Ohmic discharges on TCV [39, 40]. Here, the ion ∇B drift was away from the primary X-point to avoid H-mode transitions. Density ramps were performed in a total of 17 configurations changing $f_x = 2 - 21$, $R_{OSP} = 0.62 - 1.06$ m, $\rho_\psi = 1.012,\ 1.036$ and $Z_{axis} = -0.11 - 0.29$ m. A change in the detachment onset has only been observed with a vertical shift of the plasma. Changes of the poloidal and total flux expansion lead to a roll over of the total ion flux at similar densities as can be seen from Figs. 10 and 11. At higher f_x the roll over seems to be more pronounced and aslo changes in the evolution of the CIII radiation front or the onset of recombination have been observed. Deviations of the R_{OSP} dependence from the standard 2 point model have been observed. The heat flux is reduced as expected, but the density decreases rather than increases leading to a higher temperature at the target than predicted. The detachment onset is not affected by R_{OSP} contradicting the expectations (Fig. 11). Hence, there is no consistent dependence on the total flux expansion. SOLPS5.0 modelling of the novel divertor currently built for MAST Upgrade comparing a conventional configuration to three Super-X configurations

showed, however, that the real advantage of the Super-X configuration only manifests itself with sufficient divertor closure [42], although in all Super-X configurations the heat load in comparison to the conventional divertor is reduced. It should be noted that not only the change in R_{OSP} in these configurations is much larger than on TCV, but also the relative change in B_t due to the tight aspect ratio configuration. The progression of C^{2+} radiation front towards the core is slowed down considerably in the "X-divertor" like configurations due to the presence of the secondary X-point similar to what is seen in a conventional divertor around the primary X-point.

6 First wall loads The heat and particle loads in the narrow region around the strike points are the most severe in future devices, but as the density is increased in present day devices a density shoulder forms far out into the SOL [46]. This broader SOL could be of concern for future devices, in particular if the ion energy is above the sputtering threshold leading to increased heat loads and impurity influx. This transport is dominantly driven by strong intermittency (filaments). The filament properties and their relation to the density shoulder formation have been investigated in L-mode on AUG [47, 48, 47, 49], MAST [50, 51, 52, 53] and TCV [54] as well as inter ELM H-mode phases on AUG [55, 47, 49] have been investigated in detail. In AUG [49] and MAST [56, 52] L-mode discharges also the ion temperature in the filaments could be measured using a retarding field energy analyser. At low density $T_i/T_e \gtrsim 3-4$ in the far SOL, whilst at higher density $T_i/T_e \sim 1$.

Multi-machine L-mode data from AUG, JET, and COMPASS in various conditions show a clear transition in filament behaviour as the effective collisionality, $\Lambda = \frac{L_{||}\nu_{ei}}{c_s}\frac{\Omega_i}{\Omega_e}$ (c_s: sound speed, Ω cyclotron frequency) in the divertor is increased above $\Lambda_{div} > 1$[48], though on COMPASS $\Lambda_{div} < 1$. The filament motion seems in broad agreement with 2D modelling [57] using cold ions [49]. The inter ELM H-mode data show that Λ_{div} may be a necessary condition comparing discharges with high D fuelling to N seeding at the same Λ_{div}. The nitrogen seeded discharges showed no shoulder formation. In Fig. 12 filament properties

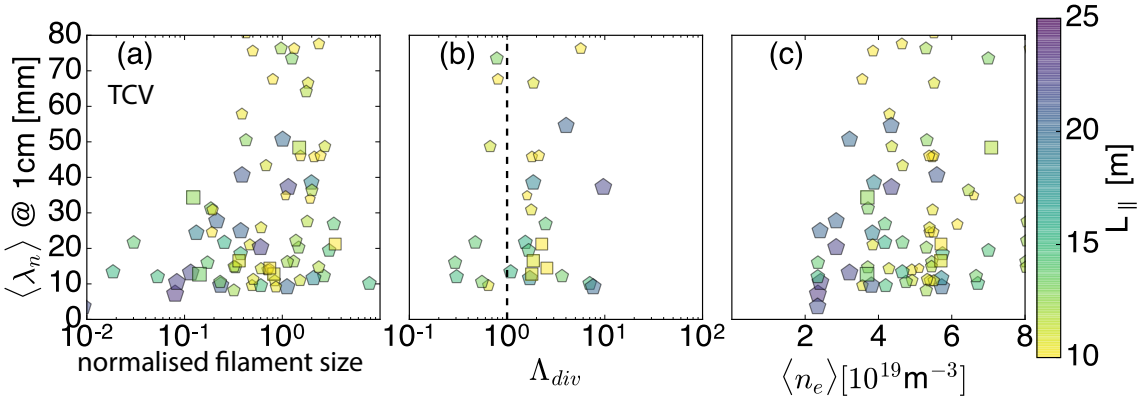

Figure 12: *Density e-folding length as a function of (a) normalised perpendicular filament size, (b) effective collisionality in the divertor and average density on TCV evaluated at 1 cm from the separatrix (⬠ DN, □ LSN).*

for various discharges on TCV are shown with the focus on the connection length $L_{||}$ dependence. This can be varied in TCV independently of q_{95} by moving the plasma up and down. This dependence is found to be rather weak. The strongest correlation is found between λ_n and filament size pointing towards the role of the turbulence. The dependence

on Λ_{div} is weaker than on AUG and JET.

The MAST L-mode data rules out divertor detachment and the ionisation source as a reason for the density shoulder formation [52]. Statistical analysis of data at different I_{p} showed that the binormal size, $\sigma_{\perp}$, decreases and the radial motion, $V_{b,r}$ of the filaments increases with $L_{||}$ [51] without showing signs of a clear transition as on AUG or JET, despite the formation of a shoulder at low I_{p}. Given that a 50% reduction in $\sigma_{\perp}$ is observed alongside a 5-fold increase in $L_{||}$, the more modest 100% increase in $v_{b,r}$ is substantially less than predicted by a sheath-dissipative scaling. Neither scaling predicts the observed change to $v_{b,r}$ which may be an indication that both inertial and sheath dissipative effects play a role in filament dynamics in MAST.

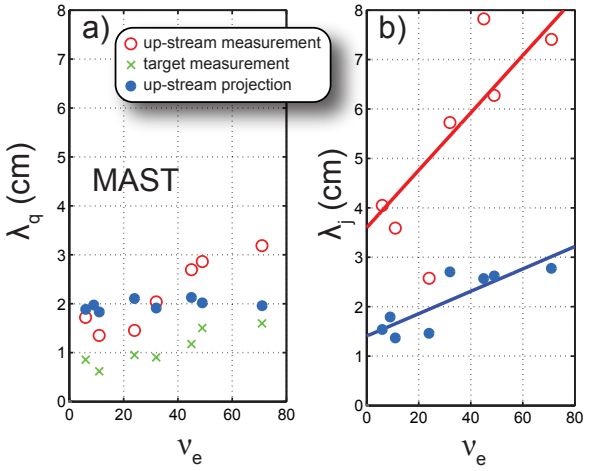

Figure 13: *Comparison of up-stream and target (a) heat flux, (b) j_{sat} e-folding length in MAST as function of electron collisionality.*

Comparing upstream SOL profiles from various measurement with target profiles [50, 52] showed that projection target values to up-stream values using a drift-based model [58] works well for heat flux width λ_q, but is not appropriate for the saturation current (see Fig. 13). Indeed the heat flux carried by the filaments in the wings of the profile is only a small fraction of the total power balance [50]. The filamentary dynamics in the mid-plane are found to be compatible with established scaling of the heat flux width λ_q.

7 Summary: Research on EU-MST has improved our understanding towards an integrated plasma-edge/wall solution. Critical questions such as ELM control, small ELM regimes, detachment control, operation in He, advanced divertor configurations and cross field SOL transport have been progressed considerably. ELM suppression has been achieved at low collisionality for the first time on AUG and the transferability of RMP ELM control from He to D has been shown. The modelling of the plasma response has been validated with several different codes. The role of the SOL density for access to small ELM regimes has been demonstrated unifying pictures at high gas fuelling and application of RMP. In particular the ITER base-line scenario has been shown to be close to the access to small ELM regimes. Future work needs to prove that such regimes are indeed possible with high SOL density, but low collisionality. The advanced divertor configurations start questioning the validity of our understanding of SOL transport (even parallel). Flux expansion has been shown to widen the detachment window with an open divertor in TCV. Modelling of the closed MAST-U divertor shows very promising reduction in target heat loads, but also stresses the importance of divertor closure. Filamentary transport leads to the formation of a broad density shoulder. Far SOL heat loads however seem to be only a fraction of the total power balance. The shoulder formation is clearly governed by a change in turbulent behaviour, but a unifying parameter characterising this transition has not been found yet.

Acknowledgements: This work has been carried out within the framework of the EUROfusion

Consortium and has received funding from the Euratom research and training programme 2014-2018 under grant agreement No 633053. The views and opinions expressed herein do not necessarily reflect those of the European Commission.

References:

[1] ZOHM, H., Plasma Phys. Control. Fusion **38** (1996) 105.
[2] KIRK, A. et al., Nuclear Fusion **54** (2014) 114012.
[3] LOEWENHOFF, T. et al., Nuclear Fusion **55** (2015) 123004.
[4] LOARTE, A. et al., Plasma Phys. Control. Fusion **45** (2003) 1549.
[5] SCHWEINZER, J. et al., Nuclear Fusion **56** (2016) 106007.
[6] BEURSKENS, M. et al., Nuclear Fusion **54** (2014) 043001.
[7] DUNNE, M. et al., in *42nd EPS Conference on Plasma Physics*, European Physical Society, 2015.
[8] STOBER, J. et al., Nucl. Fusion **41** (2001) 1123.
[9] EICH, T. et al., in *Proceedings of the 22nd International Conference on Plasma Surface Interactions in Controlled Fusion Devices (22nd PSI) , 30 May - 3rd June, Rome, Italy*, 2016.
[10] KIRK, A. et al., Nuclear Fusion **55** (2015) 043011.
[11] VALOVIČ, M. et al., Nuclear Fusion **56** (2016) 066009.
[12] LEYLAND, M. et al., Nuclear Fusion **55** (2015) 013019.
[13] DUNNE, M. et al., in *Proceedings of the 43rd EPS Conference on Plasma Physics, 4 - 8 July 2016, Leuven, Belgium*, volume 40A of *europhysics conference abstracts*, EPS, 2016.
[14] LENNHOLM, M. et al., Nuclear Fusion **55** (2015) 063004.
[15] SUTTROP, W. et al., in *Proceedings of the 43rd EPS Conference on Plasma Physics, 4 - 8 July 2016, Leuven, Belgium*, volume 40A of *europhysics conference abstracts*, EPS, 2016.
[16] LEUTHOLD, N. et al., submitted to Plasma. Phys. Control. Fusion.
[17] OSBORNE, T. H. et al., in *Europhysics Conference Abstracts (Proc. of the 24th EPS Conference on Controlled Fusion and Plasma Physics, Berchtesgaden,1997)*, edited by SCHITTENHELM, W. et al., volume 21A, part III, pages 1101–1105, EPS secretariat, 6 rue des Frères Lumière 68200 Mulhouse France, 1997, European Physical Society.
[18] LIU, Y. et al., Nuclear Fusion **56** (2016) 056015.
[19] RYAN, D. A. et al., Plasma Physics and Controlled Fusion **57** (2015) 095008.
[20] LI, L. et al., Nuclear Fusion **56** (2016) 126007.
[21] RYAN, D. et al., submitted to Plasma Phys. Control. Fusion.
[22] WILLENSDORFER, M. et al., arXiv preprint arXiv:1603.09150 (2016).
[23] ORAIN, F. et al., in *Proceedings of the 43rd EPS Conference on Plasma Physics, 4 - 8 July 2016, Leuven, Belgium*, volume 40A of *europhysics conference abstracts*, EPS, 2016.
[24] MINK, F. et al., in *Proceedings of the 43rd EPS Conference on Plasma Physics, 4 - 8 July 2016, Leuven, Belgium*, volume 40A of *europhysics conference abstracts*, EPS, 2016.
[25] VANOVAC, B. et al., in *Proceedings of the 43rd EPS Conference on Plasma Physics, 4 - 8 July 2016, Leuven, Belgium*, volume 40A of *europhysics conference abstracts*, EPS, 2016.
[26] SUTTROP, W. et al., Phys. Rev. Lett. **106** (2011) 225004.
[27] WOLFRUM, E. et al., in *42nd EPS Conference on Plasma Physics, 22 - 26 June 2015, Lisbon Portugal*, volume 39 E of *europhysics conference abstracts*, European Physical Society, 2015.
[28] LANG, P. et al., Nuclear Fusion **53** (2013) 043004.
[29] KOCSIS, G. et al., in *42nd EPS Conference on Plasma Physics*, European Physical Society, 2015.
[30] SCHNEIDER, P. A. et al., Plasma Physics and Controlled Fusion **56** (2014) 025011.
[31] FRASSINETTI, L. et al., submitted to Nucl. Fusion.
[32] KIRK, A. et al., Journal of Physics: Conference Series **123** (2008) 012012.
[33] BERNERT, M. et al., Plasma Physics and Controlled Fusion **57** (2015) 014038.
[34] KALLENBACH, A. et al., Plasma Physics and Controlled Fusion **52** (2010) 055002.
[35] BERNERT, M. et al., in *Proceedings of the 22nd International Conference on Plasma Surface Interactions in Controlled Fusion Devices (22nd PSI) , 30 May - 3rd June, Rome, Italy*, 2016.
[36] REIMOLD, F. et al., in *Proceedings of the 22nd International Conference on Plasma Surface Interactions in Controlled Fusion Devices (22nd PSI) , 30 May - 3rd June, Rome, Italy*, 2016.
[37] FAITSCH, M. et al., in *Proceedings of the 22nd International Conference on Plasma Surface Interactions in Controlled Fusion Devices (22nd PSI) , 30 May - 3rd June, Rome, Italy*, 2016.
[38] BRIDA, D. et al., in *Proceedings of the 22nd International Conference on Plasma Surface Interactions in Controlled Fusion Devices (22nd PSI) , 30 May - 3rd June, Rome, Italy*, 2016.
[39] THEILER, C. et al., Submitted to Nucl. Fusion.
[40] REIMERDES, S. et al., in *Proceedings of the 26th IAEA Fusion Energy Conference, 17-22 October, Kyoto, Japan*, 2016.
[41] HAVLÍČKOVÁ, E. et al., Plasma Physics and Controlled Fusion **56** (2014) 075008.
[42] HAVLÍČKOVÁ, E. et al., Plasma Physics and Controlled Fusion **57** (2015) 115001.
[43] LUNT, T. et al., Plasma Physics and Controlled Fusion **58** (2016) 045027.
[44] LABIT, B. et al., in *Proceedings of the 22nd International Conference on Plasma Surface Interactions in Controlled Fusion Devices (22nd PSI) , 30 May - 3rd June, Rome, Italy*, 2016.
[45] CANAL, G. et al., Nuclear Fusion **55** (2015) 123023.
[46] LABOMBARD, B. et al., Physics of Plasmas **8** (2001) 2107.
[47] CARRALERO, D. et al., in *Proceedings of the 22nd International Conference on Plasma Surface*

Interactions in Controlled Fusion Devices (22nd PSI) , 30 May - 3rd June, Rome, Italy, 2016.
[48] CARRALERO, D. et al., Phys. Rev. Lett. **115** (2015) 215002.
[49] CARRALERO, D. et al., in *Proceedings of the 26th IAEA Fusion Energy Conference, 17-22 October, Kyoto, Japan*, 2016.
[50] THORNTON, A. J. et al., Plasma Physics and Controlled Fusion **57** (2015) 115010.
[51] KIRK, A. et al., Plasma Physics and Controlled Fusion **58** (2016) 085008.
[52] MILITELLO, F. et al., Nuclear Fusion **56** (2016) 016006.
[53] MILITELLO, F. et al., in *Proceedings of the 26th IAEA Fusion Energy Conference, 17-22 October, Kyoto, Japan*, 2016.
[54] VIANELLO, N. et al., in *Proceedings of the 26th IAEA Fusion Energy Conference, 17-22 October, Kyoto, Japan*, 2016.
[55] MüLLER, H. et al., Journal of Nuclear Materials **463** (2015) 739 .
[56] ALLAN, S. Y. et al., Plasma Physics and Controlled Fusion **58** (2016) 045014.
[57] THEILER, C. et al., Phys. Rev. Lett. **103** (2009) 065001.
[58] EICH, T. et al., Phys. Rev. Lett. **107** (2011) 215001.

Appendix 1: The EUROfusion MST1 Team

J. Adamek[30], M. Agostini[8], D. Aguiam[31], J. Ahn[6], L. Aho-Mantila[56], R. Akers[5], R. Albanese[52], R. Aledda[11], E. Alessi[24], S. Allan[5], D. Alves[31], R. Ambrosino[53], L. Amicucci[45], H. Anand[16], G. Anastassiou[41], Y. Andrèbe[16], C. Angioni[38], G. Apruzzese[45], M. Ariola[53], H. Arnichand[6], W. Arter[5], A. Baciero[36], M. Barnes[43], L. Barrera[19,46], R. Behn[16], A. Bencze[57], J. Bernardo[31], M. Bernert[38], P. Bettini[8], M. Beurskens[5], P. Bilkova[30], P. Bilková[30], W. Bin[24], G. Birkenmeier[38], J. Bizarro[31], P. Blanchard[16], T. Blanken[17], M. Bluteau[14], V. Bobkov[38], O. Bogar[30], P. Böhm[30], T. Bolzonella[8], Luca Boncagni[45], A. Botrugno[45], C. Bottereau[6], F. Bouquey[6], C. Bourdelle[6], S. Brémond[6], S. Brezinsek[21], D. Brida[38], F. Brochard[47], J. Buchanan[5], H. Bufferand[6], P. Buratti[45], P. Cahyna[30], G. Calabrò[45], Y. Camenen[2], R. Caniello[24], B. Cannas[11], A. Canton[8], A. Cardinali[45], D. Carnevale[54], M. Carr[5], D. Carralero[38], P. Carvalho[31], L. Casali[38], C. Castaldo[45], F. Castejón[36], R. Castro[36], F. Causa[45], R. Cavazzana[8], M. Cavedon[38], M. Cecconello[12], S. Ceccuzzi[45], R. Cesario[45], C.D. Challis[5], I.T. Chapman[5], S. Chapman[7], M. Chernyshova[29], D. Choi[16], C. Cianfarani[45], G. Ciraolo[6], J. Citrin[20], F. Clairet[6], I. Classen[20], S. Coda[16], R. Coelho[31], J.W. Coenen[21], L. Colas[6], G. Conway[38], Y. Corre[6], S. Costea[26], F. Crisanti[45], N. Cruz[31], G. Cseh[57], A. Czarnecka[29], O. D'Arcangelo[45], M. De Angeli[24], G. de masi[8], G. De Temmerman[32], G. De Tommasi[52], J. Decker[16], R.S. Delogu[8], R. Dendy[5], P. Denner[21], C. Di Troia[45], M. Dimitrova[30], R. D'Inca[38], V. Dorić[55], D. Douai[6], A. Drenik[33,38], B. Dudson[58], D. Dunai[57], M. Dunne[38], B.P. Duval[16], L. Easy[5], T. Eich[38], S. Elmore[5], B. Erdős[28], B. Esposito[45], E. Fable[38], M. Faitsch[38], A. Fanni[11], N. Fedorczak[6], F. Felici[17], J. Ferreira[31], O. Fevrier[6], O. Février[6], O. Ficker[30], S. Fietz[38], L. Figini[24], A. Figueiredo[31], A. Fil[6], G. Fishpool[5], M. Fitzgerald[5], M. Fontana[16], O. Ford[39], L. Frassinetti[23], R. Fridström[23], D. Frigione[45], G. Fuchert[38], C. Fuchs[38], M. Furno Palumbo[8], S. Futatani[4], L. Gabellieri[45], K. Gałązka[29], J. Galdon[46], J. Galdon-Quiroga[46], S. Galeani[54], D. Gallart[4], A. Gallo[6], C. Galperti[16,24], Y. Gao[21], S. Garavaglia[24], J. Garcia[6], A. Garcia-Carrasco[23], J. Garcia-Lopez[46], M. Garcia-Munoz[46], J.-L. Gardarein[2], L. Garzotti[5], J. Gaspar[2], Eric Gauthier[6], P. Geelen[17], B. Geiger[38], P. Ghendrih[6], F. Ghezzi[24],

L. Giacomelli[24], L. Giannone[38], E. Giovannozzi[45], C. Giroud[5], C. Gleason González[34], M. Gobbin[8], T.P. Goodman[16], G. Gorini[50], M. Gospodarczyk[54], G. Granucci[24], M. Gruber[38], A. Gude[38], L. Guimarais[31], R. Guirlet[6], J. Gunn[6], P. Hacek[30], S. Hacquin[6], A. Hakola[56], S. Hall[5], C. Ham[5], T. Happel[38], J. Harrison[5], D. Harting[5], V. Hauer[34], E. Havlickova[5], T. Hellsten[23], W. Helou[6], S. Henderson[14], P. Hennequin[35], M. Heyn[27], B. Hnat[43], D. Hogeweij[20], C. Honoré[35], C. Hopf[38], J. Horáček[30], G. Hornung[9], L. Horváth[28], Z. Huang[16], A. Huber[21], J. Igitkhanov[34], V. Igochine[38], M. Imrisek[30], P. Innocente[8], C. Ionita-Schrittwieser[26], H. Isliker[3], I. Ivanova-Stanik[29], A.S. Jacobsen[44], P. Jacquet[5], M. Jakubowski[39], A. Jardin[6], F. Jaulmes[20], F. Jenko[38], T. Jensen[44], O. Jeppe Miki Busk[44], M. Jessen[44], E. Joffrin[6], O. Jones[5], T. Jonsson[23], A. Kallenbach[38], N. Kallinikos[3], S. Kálvin[57], A. Kappatou[38,20], J. Karhunen[1], A. Karpushov[16], S. Kasilov[27], G. Kasprowicz[29], A. Kendl[26], W. Kernbichler[27], D. Kim[16], A. Kirk[5], S. Kjer[44], I. Klimek[12], G. Kocsis[57], D. Kogut[6], M. Komm[30], S.B. Korsholm[44], H.R. Koslowski[21], M. Koubiti[2], J. Kovacic[33], K. Kovarik[30,43], N. Krawczyk[29], J. Krbec[30], K. Krieger[38], A. Krivska[37], R. Kube[26], O. Kudlacek[8,38], T. Kurki-Suonio[1], B. Labit[16], F.M. Laggner[25], L. Laguardia[24], A. Lahtinen[51], P. Lalousis[22], P. Lang[38], P. Lauber[38], N. Lazányi[28], A. Lazaros[41], H.B. Le[16], A. Lebschy[38], J. Leddy[58], L. Lefévre[48], M. Lehnen[32], F. Leipold[44], A. Lessig[38], M. Leyland[58], L. Li[21], Y. Liang[21], B. Lipschultz[58], Y.Q. Liu[5], T. Loarer[6], A. Loarte[32], T. Loewenhoff[21], B. Lomanowski[13], V.P. Loschiavo[52], T. Lunt[38], I. Lupelli[13], H. Lux[5], A. Lyssoivan[37], J. Madsen[44], P. Maget[6], C. Maggi[5], R. Maggiora[42], M.L. Magnussen[44], J. Mailloux[5], B. Maljaars[17], A. Malygin[16], P. Mantica[24], M. Mantsinen[4,59], M. Maraschek[38], B. Marchand[51], N. Marconato[8], C. Marini[16], M. Marinucci[45], T. Markovic[30], D. Marocco[45], L. Marrelli[8], P. Martin[8], Y. Martin[16], J. R. Martin Solis[36], A. Martitsch[27], S. Mastrostefano[53,18], M. Mattei[52], G. Matthews[5], M. Mavridis[3], M.-L. Mayoral[19,5], D. Mazon[6], P. Mc Carthy[49], R. McAdams[5], G. McArdle[5], P. McCarthy[49], K. McClements[5], R. McDermott[38], B. McMillan[7], G. Meisl[38], A. Merle[16], H. Meyer[5], O. Meyer[6], D. Milanesio[42], F. Militello[5], I.G. Miron[40], K. Mitosinkova[30], J. Mlynar[30], A. Mlynek[38], D. Molina[6], P. Molina[16], I. Monakhov[5], J. Morales[6], D. Moreau[6], P. Morel[35], J.-M. Moret[16], A. Moro[24], D. Moulton[5], H.W. Müller[38], F. Nabais[31], E. Nardon[6], V. Naulin[44], A. Nemes-Czopf[28], F. Nespoli[16], R. Neu[38], A.H. Nielsen[44], S. K. Nielsen[44], V. Nikolaeva[31], S. Nimb[44], M. Nocente[50], R. Nouailletas[6], S. Nowak[24], M. Oberkofler[38], M. Oberparleiter[10], R. Ochoukov[38], T. Odstrčil[38], J. Olsen[44], J. Omotani[5], M.G. O'Mullane[14], F. Orain[38,6], N. Osterman[33], R. Paccagnella[8], S. Pamela[5], L. Pangione[5], M. Panjan[33], G. Papp[38], R. Papřok[30], V. Parail[5], F. I. Parra[43], A. Pau[11], G. Pautasso[38], S.-P. Pehkonen[56], A. Pereira[36], E. Perelli Cippo[24], V. Pericoli Ridolfini[53], M. Peterka[30], P. Petersson[23], V. Petrzilka[30], P. Piovesan[8], C. Piron[8], A. Pironti[52], F. Pisano[11], T. Pisokas[3], R. Pitts[32], I. Ploumistakis[22], V. Plyusnin[31], G. Pokol[28], D. Poljak[55], P. Pölöskei[28], Z. Popovic[36], G. Pór[28], L. Porte[16], S. Potzel[38], I. Predebon[8], M. Preynas[16],

G. Primc[33], G. Pucella[45], M.E. Puiatti[8], T. Pütterich[38], M. Rack[21], G. Ramogida[45], C. Rapson[38], J.Juul Rasmussen[44], J. Rasmussen[44], G.A. Rattá[36], S. Ratynskaia[23], G. Ravera[45], D. Réfy[57], M. Reich[38], H. Reimerdes[16], F. Reimold[21,38], M. Reinke[58], D. Reiser[21], M. Resnik[33], C. Reux[6], D. Ripamonti[24], D. Rittich[38], G. Riva[24], M. Rodriguez-Ramos[46], V. Rohde[38], J. Rosato[35], F. Ryter[38], S. Saarelma[5], R. Sabot[6], F. Saint-Laurent[6], M. Salewski[44], A. Salmi[56], D. Samaddar[5], L. Sanchis-Sanchez[46], J. Santos[31], O. Sauter[16], R. Scannell[5], M. Scheffer[20], M. Schneider[6,32], B. Schneider[26], P. Schneider[38], M. Schneller[38], R. Schrittwieser[26], M. Schubert[38], J. Schweinzer[38], J. Seidl[30], M. Sertoli[38], S. Šesnić[55], A. Shabbir[9], A. Shalpegin[6], B. Shanahan[58], S. Sharapov[5], U. Sheikh[16], G. Sias[11], B. Sieglin[38], C. Silva[31], A. Silva[31], M. Silva Fuglister[16], J. Simpson[5], A. Snicker[1], C. Sommariva[6], C. Sozzi[24], S. Spagnolo[8], G. Spizzo[8], M. Spolaore[8], T. Stange[39], M. Stejner[44], M. Stejner Pedersen[44], I. Stepanov[9], J. Stober[38], P. Strand[10], A. Šušnjara[55], W. Suttrop[38], T. Szepesi[57], B. Tál[57], T. Tala[56], P. Tamain[6], G. Tardini[38], M. Tardocchi[24], A. Teplukhina[16], D. Terranova[8], D. Testa[16], C. Theiler[16], A. Thornton[5], P. Tolias[23], L. Tophøj[44], W. Treutterer[38], G.L. Trevisan[8], M. Tripsky[37], C. Tsironis[41], C. Tsui[16], O. Tudisco[45], A. Uccello[24], J, Urban[30], M. Valisa[8], P. Vallejos[23], M. Valovic[5], H. Van den Brand[20], B. Vanovac[20], S. Varoutis[34], S. Vartanian[6], J. Vega[36], G. Verdoolaege[9], K. Verhaegh[58], L. Vermare[35], N. Vianello[16,8], J. Vicente[31], E. Viezzer[38], L. Vignitchouk[23], W.A.J. Vijvers[20,16], F. Villone[18], B. Viola[45], L. Vlahos[3], I. Voitsekhovitch[19,5], P. Vondráček[30], N.M.T. Vu[6], D. Wagner[38], N. Walkden[5], N. Wang[21], T. Wauters[37], M. Weiland[38], V. Weinzettl[30], E. Westerhof[20], M. Wiesenberger[26], M. Willensdorfer[38], M. Wischmeier[38], I. Wodniak[12], E. Wolfrum[38], D. Yadykin[12], R. Zagórski[29], I. Zammuto[38], P. Zanca[8], R. Zaplotnik[33], P. Zestanakis[41], W. Zhang[9], S. Zoletnik[57], M. Zuin[8]

[1]Aalto University, Department of Applied Physics, P.O.Box 14100, FI-00076 Aalto, Finland,
[2]Aix-Marseille Université, CNRS, PIIM, F13013 Marseille, France,
[3]Aristotle University of Thessaloniki, Thessaloniki, Greece,
[4]Barcelona Supercomputing Center, Jordi Girona 29, 08034 Barcelona, Spain,
[5]CCFE, Culham Science Centre, Abingdon, Oxon, OX14 3DB, UK,
[6]CEA, IRFM, F-13108 Saint Paul Lez Durance, France,
[7]Centre for Fusion, Space and Astrophysics, Department of Physics, Warwick University, Coventry CV4 7AL, UK,
[8]Consorzio RFX, corso Stati Uniti 4, 35127 Padova, Italy,
[9]Department of Applied Physics UG (Ghent University) St-Pietersnieuwstraat 41 B-9000 Ghent Belgium,
[10]Department of Earth and Space Sciences, Chalmers University of Technology, SE-41296 Gothenburg, Sweden,
[11]Department of Electrical and Electronic Engineering, University of Cagliari, Piazza d'Armi 09123 Cagliari, Italy,

[12]Department of Physics and Astronomy, Uppsala University, SE-75120 Uppsala, Sweden,
[13]Department of Physics, Durham University, Durham, DH1 3LE, UK,
[14]Department of Physics, University of Strathclyde, 107 Rottenrow, Glasgow G4 0NG, UK,
[15]Durham University,
[16]Ecole Polytechnique Fédérale de Lausanne (EPFL), Swiss Plasma center (SPC), CH-1015 Lausanne, Switzerland,
[17]Eindhoven, University of Technology P.O. Box 513 NL-5600 MB Eindhoven, The Netherlands,
[18]ENEA/CREATE, DIEI, Università di Cassino, Via Di Biasio 43, 03043, Cassino (FR), Italy,
[19]EUROfusion PMU, Boltzmannstraße 2, 85748, Garching, Germany,
[20]FOM Institute DIFFER P.O. Box 1207 NL-3430 BE Nieuwegein, The Netherlands,
[21]Forschungszentrum Jülich GmbH, Institut für Energie- und Klimaforschung - Plasmaphysik, 52425 Jülich, Germany,
[22]Foundation of Research and Technology, Crete, Greece ,
[23]Fusion Plasma Physics, EES, KTH, SE-10044 Stockholm, Sweden,
[24]IFP-CNR, via R. Cozzi 53, 20125 Milano, Italy,
[25]Institut für Angewandte Physik, Technische Universität Wien, Wiedner Hauptstraße 8-10, 1040 Wien,
[26]Institut für Ionen- und Angewandte Physik, Universität Innsbruck, Technikerstraße 25, 6020 Innsbruck,
[27]Institut für Theoretische Physik, Technische Universität Graz, 8010 Graz,
[28]Institute of Nuclear Techniques, Budapest University of Technology and Economics, P.O.Box 91, H-1521 Budapest, Hungary,
[29]Institute of Plasma Physics and Laser Microfusion, Hery 23, 01-497 Warsaw, Poland,
[30]Institute of Plasma Physics AS CR, Za Slovankou 1782/3, 182 00 Praha 8, Czech Republic,
[31]Instituto de Plasmas e Fusão Nuclear, Instituto Superior Técnico, Universidade de Lisboa, Portugal,
[32]ITER Organization, Route de Vinon, CS 90 046, 13067 Saint Paul Lez Durance, France,
[33]Jožef Stefan Institute, Jamova 39, SI-1000 Ljubljana, Slovenia,
[34]Karlsruhe Institute of Technology, P.O.Box 3640, D-76021 Karlsruhe, Germany,
[35]Laboratoire de Physique des Plasmas, CNRS UMR7648, Ecole Polytechnique, 91128 Palaiseau, France,
[36]Laboratorio Nacional de Fusión, CIEMAT, Madrid, Spain,
[37]Laboratory for Plasma Physics Koninklijke Militaire School - Ecole Royale Militaire Renaissancelaan 30 Avenue de la Renaissance B-1000, Brussels, Belgium,
[38]Max-Planck-Institut für Plasmaphysik, D-85748 Garching, Germany,
[39]Max-Planck-Institut für Plasmaphysik, Teilinstitut Greifswald, D-17491 Greifswald, Germany,
[40]National Institute for Laser, Plasma and Radiation Physics, P.O.Box MG-36, Bucharest, Romania,

[41]National Technical University of Athens, Athens, Greece,
[42]Politecnico di Torino, Dipartimento di Elettronica e Telecomunicazioni (DET), Torino, Italy,
[43]Rudolf Peierls Centre for Theoretical Physics, University of Oxford, Oxford, UK Culham Centre for Fusion Energy, Abingdon, UK,
[44]Technical University of Denmark, Department of Physics, Bldg 309, DK-2800 Kgs Lyngby, Denmark,
[45]Unità Tecnica Fusione - ENEA C. R. Frascati - via E. Fermi 45, 00044 Frascati (Roma), Italy,
[46]Universidad de Sevilla, Sevilla, Spain,
[47]Université de Lorraine, Institut Jean Lamour, Vandoeuvre-lés-Nancy, 54000 Nancy, France,
[48]Université Grenoble Alpes, LCIS, F26902 Valence, France,
[49]University College Cork (UCC), Ireland,
[50]University Milano-Bicocca, piazza della Scienza 3, 20126 Milano, Italy,
[51]University of Helsinki, Department of Physics, P.O.Box 64, FI-00014 University of Helsinki, Finland,
[52]University of Napoli 'Federico II', Consorzio CREATE, Via Claudio 21, 80125 Napoli, Italy,
[53]University of Napoli Parthenope, Consorzio CREATE, Via Claudio 21, 80125 Napoli, Italy,
[54]University of Rome Tor Vergata, via del Politecnico 1, 00133 Rome, Italy,
[55]University of Split, Faculty of Electrical Engineering, Mechanical Engineering and Naval Architecture, R. Boskovica 32, 21 000 Split, Croatia,
[56]VTT Technical Research Centre of Finland, P.O.Box 1000, FI-02044 VTT, Finland,
[57]Wigner Research Centre for Physics, P.O.B. 49, H - 1525 Budapest, Hungary,
[58]York Plasma Institute, Department of Physics, University of York, Heslington, York, YO10 5DD, UK
[59]ICREA, Pg. Lluís Companys 23, 08010 Barcelona, Spain.